ON THE TRANSITION IN SPANWISE INSTABILITY RELAMINARIZATION IN THE WAKE OF OSCILLATING FOILS

Suyash Verma & Arman Hemmati*
Department of Mechanical Engineering, University of Alberta, Edmonton, AB, Canada T6G 2R3
* arman.hemmati@ualberta.ca

ABSTRACT

The wake of an oscillating hydrofoil in combined heaving and pitching motion is numerically evaluated at a range of reduced frequency ($0.32 \leq f^* \leq 0.64$) and phase offset ($90^\circ \leq \phi \leq 270^\circ$) at Reynolds number of $Re = 8000$. At $\phi = 90^\circ$, the growth of a secondary hairpin-like vortex system is associated with an elliptic instability, prompted by the paired primary and secondary leading edge vortices (LEV), which remains persistent within the entire range of St_c. Further, at $St_c = 0.32$, a relaminarization state of spanwise instability is evident where the LEV fails to reveal any dominant spatio-temporal growth of vortex dislocations. However, an increase in St_c to 0.40 depicts an enhancement in LEV undulation amplitude and its subsequent transformation to another hairpin-like formation later in the wake. A unique role of the counter-rotating trailing edge vortex *roller* (TEVs) is believed to trigger the transition of instability relaminarization state (at $St_c = 0.32$) in LEV, to the dominant secondary streamwise structure arrangement. Particularly, TEVs at increasing St_c intensify the vortex compression and stretching ($|<\Omega_x S_{xx}>|$) in localized regions along the LEV span that consequently promotes the vortex tearing mechanism of primary LEV. This induces its transformation to hairpin-like structures. The stability of the wake configurations is assessed using dynamic mode decomposition (DMD), which detects a neutrally stable condition at the primary forcing frequency and its harmonics.

INTRODUCTION

Vortex dynamics and interactions have captivated the fluid mechanics and turbulence community for decades (Leweke *et al.*, 2016). Understanding the formation, evolution, and early dissipation of straight vortical filaments, particularly in the wakes of aircraft and submarines, is crucial for mitigating wake-related hazards and noise propagation (Leweke & Williamson, 1998; Ortega *et al.*, 2003). The study of wake instabilities is also motivated by their relevance to the propulsive efficiency of natural bird flights and swimming mammals (Sun *et al.*, 2018). According to Deng & Caulfield (2015), the transition from symmetric reverse Von Kármán ($rBvK$) to deflected wake modes coincides with the emergence of three-dimensional instability features and enhanced thrust generation. This investigation expands our understanding of the relationship between vortex instability characteristics and three-dimensionality in turbulent wakes generated by oscillating rigid foils.

Recent research has identified a correlation between the development of secondary hairpin-like vortex structures and the motion characteristics of foils undergoing combined heaving and pitching motions (Verma & Hemmati, 2021; Verma *et al.*, 2023). The transition from heave-dominated to pitch-dominated kinematics corresponds to changes in flow dynamics that influence the growth or absence of these secondary structures (Verma *et al.*, 2023). Studies have previously reported stronger deformation of primary leading-edge vortices (LEVs) at higher chord- and amplitude-based Strouhal numbers (St_c and St_A) (Chiereghin *et al.*, 2020; Verma & Hemmati, 2021), although the connection with secondary structures remains unclear.

Investigation by Verma & Hemmati (2021) revealed dominance of elliptic-type short wavelength instability in highly propulsive wakes (Leweke & Williamson, 1998). The study also demonstrated evidence on the emergence of tongue-like dislocations on the primary *rollers*. In addition, wakes corresponding to large thrust generation were characterized by interconnected hairpin-horseshoe type structures (Verma & Hemmati, 2021). The quantitative analysis including spanwise wavelength (λ_z) and periodicity of streamwise vortex arrangement established a vivid link to the elliptic-type short wavelength instability. This association was also observed across a range of chord-based St_c and ϕ (Verma & Hemmati, 2023; Verma *et al.*, 2023). Particularly, the growth of secondary hairpin-like structures and its correspondence to spanwise instability of *rollers* and oscillating foil kinematics was discussed (Verma *et al.*, 2023). Visbal (2009) also emphasized the significant impact of varying St_c on the dynamics of LEVs. Notably, higher St_c were found to coincide with substantial deformations of the LEV and its subsequent transition to arched vortex undulation pattern (Visbal, 2009). In a recent study by Son *et al.* (2022), LEV instabilities were examined in the context of heaving oscillations for both high aspect ratio wings and infinite-span foils. The study revealed changes in the strength of primary LEV and TEV in response to variations in St_c, which also coincided with alterations in the onset mechanisms of spanwise instability.

In this study, we expand on a unique mechanism that explains the transition of spanwise LEV instability to hairpin-like structures in the wake. Our objective is to fundamentally understand the mechanism of this transition as aspects of kinematics change for the oscillating foil in coupled heaving and pitching motion. The observations will provide fundamental insights and hints with regards to the association of LEV dynamics and growth of secondary structures in the wake. We further evaluate the stability characteristics of two different systems of secondary hairpin-like structures identified. The methodology for conducting the numerical study is briefly highlighted in the Problem Description, followed by assessment of major observations in the Results & Discussion section. A brief summary of important findings is then pre-

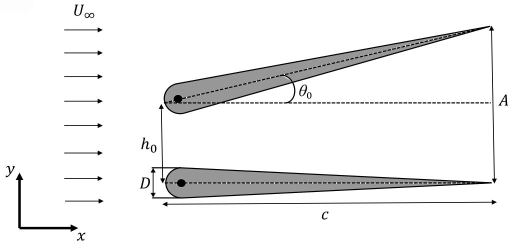

Figure 1: Schematic representing teardrop foil geometry and kinematics

sented in the Conclusions section.

PROBLEM DESCRIPTION

Three-dimensional wake evolution of an oscillating hydrofoil is assessed by solving the Navier-Stokes equations directly at $Re = 8000$. Overset Grid Assembly (OGA) method, implemented in OpenFOAM, was employed for simulating the combined heaving and pitching motion of the foil. The infinite span of the oscillating teardrop foil (see Figure 1) preserves the developing spanwise instability on primary vortex (*rollers*) and secondary structures (*ribs*) in the wake (Mittal & Balachandar, 1995; Verma & Hemmati, 2021). The heaving and pitching motion of the foil can be mathematically expressed as:

$$h = h_o \sin 2\pi f t \tag{1}$$

$$\theta(t) = \theta_o \sin(2\pi f t + \phi) \tag{2}$$

Here, the oscillation frequency (f) can be expressed in terms of the reduced frequency $St_c = fc/U_\infty$, which varied as 0.32 $\leq f^* \leq 0.56$. This corresponds to an amplitude based Strouhal number ($St_A = 2fA/U_\infty$) in the range of $0.2 \leq St_A \leq 0.6$, which further coincide with highly propulsive wakes observed for foils in coupled motion at a similar range of St_A (Schnipper *et al.*, 2009). The phase offset (ϕ) was varied in the range of $90^\circ \leq \phi \leq 270^\circ$, which ensured a heave dominated kinematics, and thereby allowing LEVs to develop and advect along the foil boundary. Contrarily, pitch dominated kinematics coincided with either a weak LEV formation or their apparent disintegration during an early stage of the oscillation cycle (Verma & Hemmati, 2021). Here, we limit the results to the case of $\phi = 90^\circ$ to mainly detail the changes in evolution of instability and secondary structures at increasing St_c.

The computational domain closely followed that of Verma & Hemmati (2023); Verma *et al.* (2023). More details on the validation and verification of the numerical methodology can be found in our previous studies (Verma & Hemmati, 2020, 2023; Verma *et al.*, 2023).

RESULTS & DISCUSSION

The mechanisms underlying the development of secondary vortex formations are qualitatively discussed at $\phi = 90^\circ$ with an increase in St_c from 0.32 to 0.56. The temporal and spatial evolution of the wake at increasing St_c is illustrated using isosurfaces of the Q-criterion, defined as $Q^+ = Qc^2/U_\infty^2$, which highlight primary leading-edge vortex (LEV) rollers, secondary streamwise structures (e.g. hairpin-like) and ribs that dominate the wake. The development of spanwise undulations on the primary LEV and their role in generating secondary hairpin-like structures is also highlighted. Particularly, beyond $St_c \geq 0.40$, a distinct transition mechanism for spanwise LEV instability is characterized by the augmented growth of secondary structures in the wake of oscillating foils. To delve deeper into the unique temporal dynamics illustrating either single or dual systems of secondary vortex structures, we compare growth rates and magnitude of dominant frequency modes using dynamic mode decomposition.

I. Transition of spanwise LEV instability

Figures 2(a) illustrate the wake corresponding to $\phi = 90^\circ$ and $St_c = 0.32$. Hairpin-like structures emerge from the secondary leading-edge vortex (LEV_s) and initially organize into a spanwise configuration (Verma & Hemmati, 2023). Shifting focus to the primary LEV ($LEV1_{ac}$ or $LEV1'_{ac}$ from the previous oscillation cycle), Figures 2(a) demonstrate its simultaneous advection with other shed trailing-edge vortices ($TEVs$) and secondary vortex structures (hairpin-like and $R1'$). $LEV1_{ac}$ exhibits pronounced undulation just before separation, while the legs of the hairpin vortex grow and form rib pairs. As $LEV1_{ac}$ continues downstream, its undulation amplitude does not substantially increase. Despite consistent elongation of rib pairs, there is no substantial increase in the bending of $LEV1'_{ac}$ at $X^+ > 5$. Therefore, the growth of secondary wake structures is attributed solely to the streamwise vorticity outflux from the LEV_s roller, as recently described by Verma *et al.* (2023) and Verma & Hemmati (2023).

A second hairpin-like system emerges as St_c increases beyond 0.32. Figure 2(b) illustrate the evolution of primary $LEV2_{ac}$ at $St_c = 0.40$, accompanied by the development of streamwise hairpin filaments near the foil trailing edge. The initiation of these secondary vortex filaments follows a mechanism similar to that described for $St_c = 0.32$ (Verma & Hemmati, 2023). However, $LEV2_{ac}$ exhibits a notably larger bending amplitude upon advection in the wake, compared to $LEV1_{ac}$ at $St_c = 0.32$. Figure 2(b) highlight the growth of another dominant system hairpin-like vortex structures (HS1$''$ and HS1$'$) along the spanwise direction at $X^+ > 2.5$. The growth of these structures appears to result from the pronounced bending and dislocations on the primary LEVs (e.g., $LEV2'_{ac}$) from previous shedding cycles. These resemble the observations of horseshoe-like formations in the wake of a stationary circular cylinder as described by Mittal & Balachandar (1995), emphasizing the mechanism of vortex core instability (Williamson, 1996). Additionally, Ryan *et al.* (2012) presented detailed observations on counter-rotating vortex pairs where the stronger vortex exhibits spanwise dislocations triggered by existing rib structures. The evolution of rib pairs is also evident in Figure 2(b), evolving in tandem with hairpin-like structures (HS1$'$ and HS1$''$). In comparison to $St_c = 0.32$, it is clear that enhanced deformation and bending of primary LEV at $St_c = 0.40$ leads to the growth of dominant hairpin-like configuration ahead of $X^+ = 5$.

Evolution of the wake at $St_c = 0.48$ and 0.56 is also shown in Figure 2(c) and 2(d), respectively. The onset of secondary hairpin-like growth near the foil trailing edge, and LEV instability, still remain prominent. The bending of the separated $LEV3_{ac}$ becomes evident at $St_c = 0.48$ in Figure 2(c). Dual hairpin-like structures become noticeable, labeled as HS2. These structures emerge due to the increasing amplification of the arch amplitude initially observed on $LEV3_{ac}$. In comparison to HS1$'$ and HS1$''$ observed at $St_c = 0.40$, the legs of HS2 elongate more rapidly at $St_c = 0.48$, wrapping

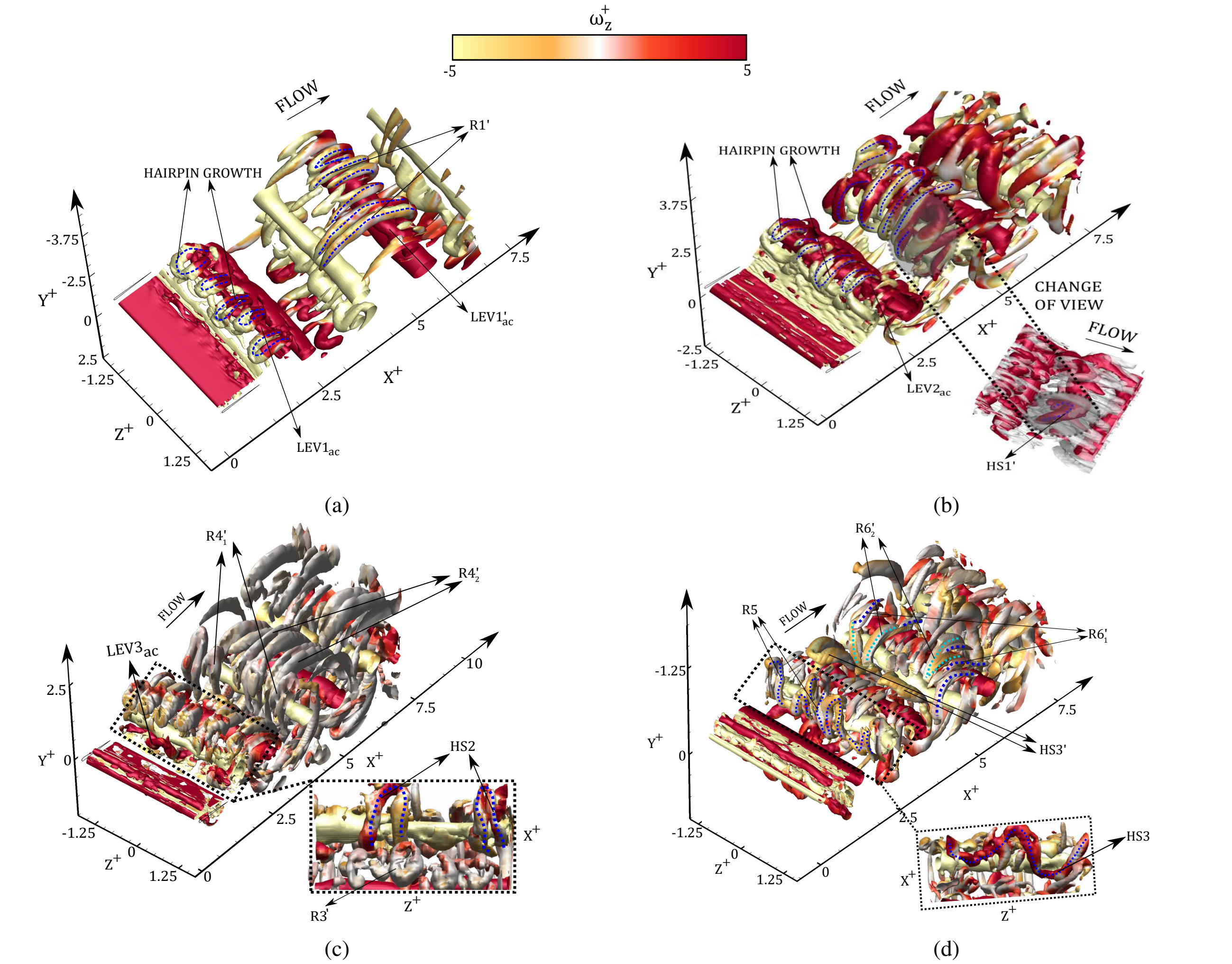

Figure 2: Wake evolution at $\phi = 90^\circ$ and $St_c = 0.32$ (a), $St_c = 0.40$ (b), $St_c = 0.48$ (c) and $St_c = 0.56$ (d). The time instants correspond to $t^+ = 0.75$. Each stage is represented using iso-surfaces of $Q^+(= 0.032)$, which are colored based on $|\omega_z^+| = 5$.

around the shed trailing-edge vortex (TEV) roller in Figure 2(c). This process leads to an early transition to a hairpin-like vortex, which then curls around its head to form ribs ($R4'_2$). Simultaneous presence of both secondary hairpin-like vortex systems in the wake is consistently observed at $St_c = 0.56$ (see Figure 2(d)). Three dominant hairpin-like structures (HS3$'$) are marked, which evolve via bending of the previously shed $LEVs$ from the bottom side of the foil. A comparable bending and transition to a dual hairpin-like system is again apparent for $LEV4_{ac}$ (shed from the top of the foil), identified as HS3. Elongated legs of hairpin-like structures formed due to vorticity outflux from the secondary LEV_s are labeled as $R5$, as they extend downstream to eventually form rib pairs, specifically R61$'$. Subsequently, HS3 breaks away from its head to form an additional system of paired rib structures downstream, labeled as R62$'$ in Figure 2(d), which elongate through the HS3$'$ system of hairpin-like structures. Overall, the wake dynamics closely resemble observations at $St_c = 0.48$, where the presence of secondary structures in the wake is attributed to two distinct mechanisms.

II. Mechanism of Instability Transition

The presented findings indicate that the primary LEV experiences high-amplitude undulation at $St_c > 0.32$, resulting in the formation of hairpin-like structures in the wake. However, further detailed analysis of the flow is required to gain a better understanding of the physical mechanism underlying this phenomenon. To this end, we focus on the principles of the vortex stretching/compression term in the vorticity budget (Wu *et al.*, 2006). This term is expressed as $\langle\Omega_x\rangle\langle S_{xx}\rangle$, where Ω_x and S_{xx} represent the vorticity and rate of strain in the streamwise direction, respectively. Depending on the positive or negative sign of this quantity, it can be interpreted as vortex stretching or compression, respectively.

The mean distribution of vortex stretching/compression is now analyzed on "focus planes" (indicated in Figures 3(a) and 3(b)) along the span of the primary LEV. This is shown in Figure 3(c) and 3(d). The planes represent localized regions around dislocations of relatively larger spatial scales, making them more susceptible to concentrated strain rates and vortex tearing (Ryan *et al.*, 2012). For $St_c = 0.32$, the planes are positioned at spanwise locations corresponding to $Z^+ = -0.21$ and $Z^+ = 1.18$ (see Figure 3(a)). It is evident that the neighboring upstream region around the primary LEV core at $t^+ = 0.5$ in Figure 3(c), exhibit localized axial vortex compression due to negative $\langle\Omega_x\rangle\langle S_{xx}\rangle$. However, the magnitude of compression reduces as the primary $LEV1_{ac}$ advects downstream in the wake at $t^+ = 0.75$. These observations are also quantitatively confirmed in Figure 3(c), corresponding to spanwise location of $Z^+ = 1.18$. The profiles of $\langle\Omega_x\rangle\langle S_{xx}\rangle$ are extracted along the streamwise direction, represented by the green dotted line on the slices shown in $\langle\Omega_x\rangle\langle S_{xx}\rangle$ contour. The temporal de-

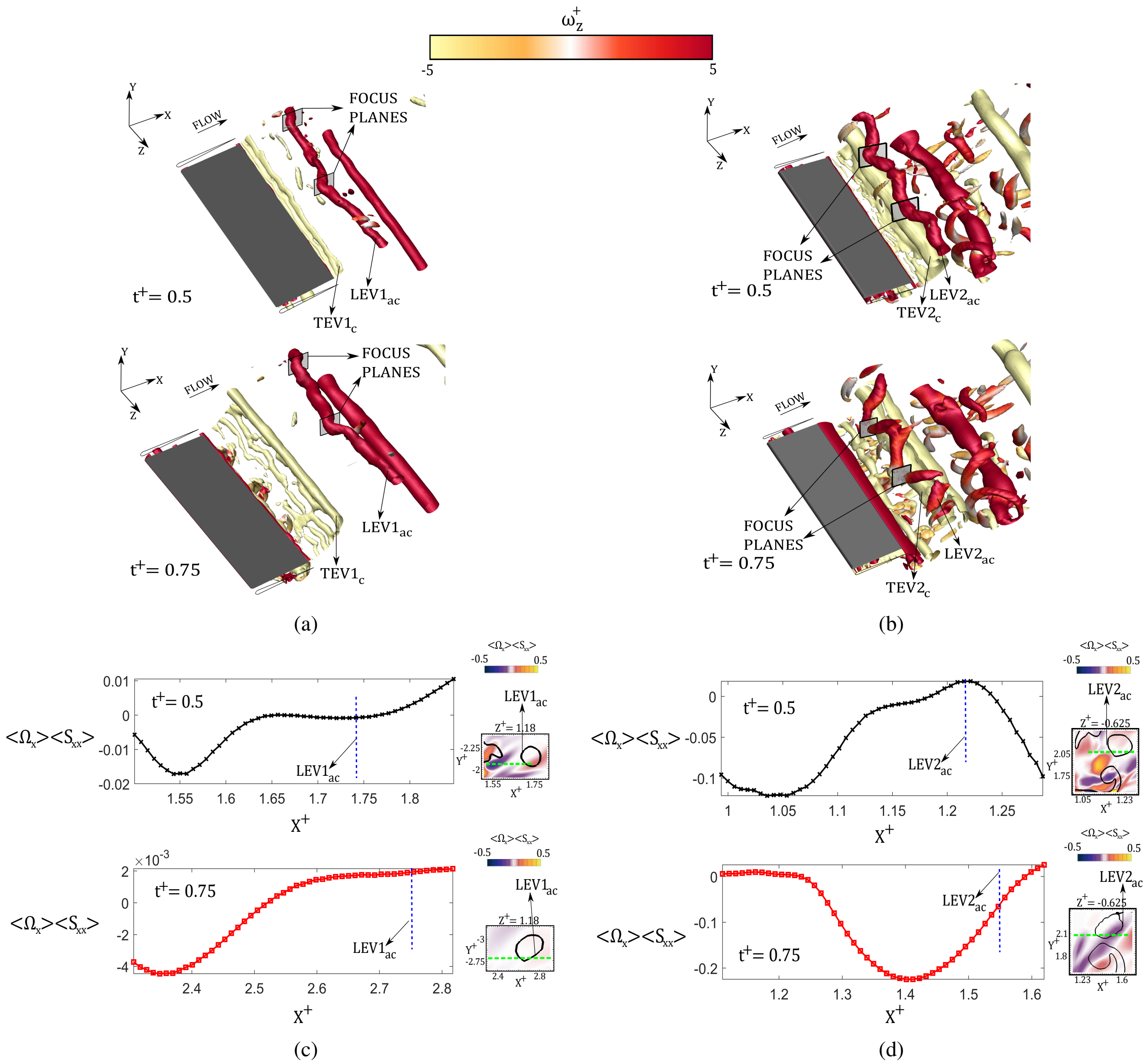

Figure 3: Wake evolution at $\phi = 90°$ and $St_c = 0.32$ (a) and $St_c = 0.40$ (b). Each stage is represented using iso-surfaces of $Q^+(= 9.6)$, which are colored based on $|\omega_z^+| = 5$. Quantitative distribution of $\langle\Omega_x\rangle\langle S_{xx}\rangle$ is shown for (c) $St_c = 0.32$ and (d) $St_c = 0.40$. The extracted data on $XY-$ planes (shown in (a) and (b)) corresponds to green dotted line marked in contours of $\langle\Omega_x\rangle\langle S_{xx}\rangle$. Black solid lines on the contours represented in (c) and (d) show the primary LEV and TEV rollers identified using $Q-$ criterion ($Q^+ = 9.6$).

crease in the magnitude of vortex compression is consistent at both spanwise locations. Particularly at $Z^+ = 1.18$, the peak magnitude of $\langle\Omega_x\rangle\langle S_{xx}\rangle$ at $t^+ = 0.75$ decreases from 0.1 (at $t^+ = 0.5$) to approximately 0.0055.

Figure 3(d) demonstrate the distribution of $\langle\Omega_x\rangle\langle S_{xx}\rangle$ at "focus planes" marked in the wake at $St_c = 0.40$ (see Figure 3(b)). The spanwise locations along the primary $LEV2_{ac}$ correspond to $Z^+ = -0.625$ and $Z^+ = 0.625$, respectively. The distribution now depicts contrasting aspects compared to the discussion presented with respect to Figure 3(c) at $St_c = 0.32$. We observe an increased compression magnitude at $t^+ = 0.75$ compared to $t^+ = 0.5$ (see Figure 3(d)). The quantitative profiles extracted in the streamwise direction for $Z^+ = -0.625$ are also shown in Figure 3(d), at $t^+ = 0.5$ and $t^+ = 0.75$ respectively. These confirm that enhanced vortex compression becomes apparent as $LEV2_{ac}$ advects downstream. This enhancement is also consistent at $Z^+ = 0.625$ (not shown here for brevity). At $Z^+ = -0.625$, the peak magnitude of $\langle\Omega_x\rangle\langle S_{xx}\rangle$ at $t^+ = 0.75$ increases from 0.125 (at $t^+ = 0.5$) to approximately 0.23. The intensified compression thus coincides with the amplification of spatial undulations, subsequently leading to localized annihilation and tearing of the $LEV2_{ac}$ core (Figure 3(b)).

Schaeffer & Le Dizés (2010) examined the nonlinear evolution of elliptic-type instability and described an instability-breakdown-relaminarization mechanism characterized by a lack of vortex core breakdown and an increase in its size on a convective time-scale. This mechanism was also studied by Ryan *et al.* (2012), who investigated numerically the perturbation growth on unequal strength counter-rotating vortex pairs. In their study, the weaker vortex from the pair underwent breakdown into streamwise filaments, while the stronger primary vortex exhibited small-scale periodic stretching due to the presence of secondary streamwise filaments (Ryan *et al.*, 2012). A similar mechanism is evident at $St_c = 0.32$, where the interaction of pre-existing hairpin-like structures with primary LEVs contributes to small-scale spanwise dislocations observed in Figure 3(a). However, at $St_c = 0.40$, in addition to

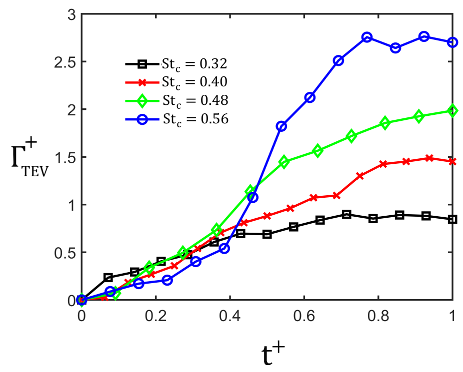

Figure 4: Variation of Γ^+_{TEV} at increasing St_c.

the occurrence of vortex dislocations due to hairpin-like structures evolving from secondary LEVs (see Figure 3(b)), the primary TEV growth in proximity to LEV results in localized intensification of compression. Consequently, the undulations continue to grow in amplitude, eventually leading to a transition from spanwise instability to its breakdown and the formation of hairpin-like structures. This intensification of compression was not observed at $St_c = 0.32$ (see Figure 3(c)). The observations at $St_c = 0.48$ and 0.56 are also consistent with those at $St_c = 0.40$. However, the results are not presented for brevity.

In addition to linking the growth of trailing-edge vortices (TEVs) with enhanced vortex compression around primary LEVs, it is noteworthy that their circulation strength ($\Gamma^+ = \Gamma/U_\infty c$) increases within the range of St_c evaluated here. This trend is depicted in Figure 4, where a pronounced increase in Γ^+_{TEV} is observed prior to $t^+ = 0.4$. This observation complements the intensification of the magnitude of $< S_{xx} >$ discussed earlier. Therefore, this phenomenon correlates the faster emergence of hairpin-like structures from the primary LEV with the amplified vortex compression reported previously.

III. DMD Analysis

To delve deeper into characterizing the two hairpin-like systems, we investigate the influence of St_c on dynamical information relevant to the growth rates of dominant DMD modes and their associated modal energy in these complex wake patterns. This analysis utilizes Dynamic Mode Decomposition (DMD) techniques (Hemati *et al.*, 2014) applied to streamwise velocity (U_x) data obtained at each St_c. Mohan *et al.* (2016) suggested that U_x significantly affects the effective angle of attack (α_{eff}), which plays a key role in governing the three-dimensionality of vortical structures on oscillating wings and foils (Visbal, 2009). A total of 270 three-dimensional unsteady snapshots within one oscillation cycle are used to compute the DMD modes, which are ranked based on their normalized energy levels. Normalization is performed using the magnitude of the highest energy mode (Mohan *et al.*, 2016). The normalized sampling rate (expressed as $\Delta t n U_\infty / c$) for the DMD input is approximately 0.00625, which according to Mohan *et al.* (2016), is sufficiently fine to capture the dominant coherent structures. Here, Δt represents the time-step size ($\Delta t = 0.0005$ s), and n denotes the number of time-steps for sampling (with $n = 10$).

We initiate the analysis by examining the frequency (f_m) and growth rate (β_m) of the most dominant DMD modes. Here, m denotes the mode number, and β_m quantifies the stability characteristics of the mode (Mohan *et al.*, 2016). A positive β_m indicates inherent instability (growth) of the mode, whereas a negative β_m signifies stability (or decay) of the mode (Zheng *et al.*, 2019). Modes with $\beta_m \approx 0$ are considered neutrally stable, suggesting sustained periodic behavior of the dominant coherent structures in this mode (Zheng *et al.*, 2019). To compute β_m, we start by calculating the logarithmic form of the eigenvalues (λ_m) for each mode. The real part of λ_m represents β_m, while the imaginary part corresponds to the frequency f_m of the mode. This is expressed mathematically as:

Table 1: Normalized mode frequencies ($St_{c,m}$) extracted from DMD for increasing St_c

St_c	Mode 1	Mode 2	Mode 3	Mode 4
0.32	0.3214	0.6355	0.9587	1.2756
0.40	0.4029	0.7972	1.1732	1.5811
0.48	0.4755	0.9522	1.4244	1.9067
0.56	0.5629	1.1321	1.6897	2.2542

$$f_m = \arctan\left(\frac{Im(\lambda_m)}{Re(\lambda_m)}\right)/(2\pi\Delta t) \tag{3}$$

$$\beta_m = \ln(Mag(\lambda_m))/\Delta t \tag{4}$$

As shown in Table 1, the normalized mode frequency (expressed in terms of $St_{c,m} = f_m * c/U_\infty$) for the first mode corresponds to the forcing frequency (St_c) of the foil oscillation. This is consistent with findings reported in literature for purely plunging (Mohan *et al.*, 2016) and pitching foils (Zheng *et al.*, 2019). The modes following Mode 1 are characterized by harmonics of the forcing frequency.

Figure 5(a) illustrates the variation of β for modes as a function of $St_{c,m}$, with St_c increasing from 0.32 to 0.56. Modes 1 to 4 exhibit nearly zero β across the entire range of St_c, suggesting a sustained periodic nature of the coherent wake structures as St_c increases. This characteristic remains consistent even in the presence of a dominant second system of hairpin-like structures at $St_c \geq 0.40$. Generally, values of β for modes beyond Mode 4 are slightly negative, indicating stability or decay. The dynamic characteristics of mode structures can be further analyzed by examining the modulus of the complex amplitude factor ($|\lambda_m|$) obtained through DMD analysis. Zheng *et al.* (2019) suggested that $|\lambda_m|$ is closely linked to the strength of vortex structures shed at the fundamental forcing frequency and its harmonics. In the context of the first 5 DMD modes, Figure 5(b) illustrates the variation of $|\lambda_m|$ corresponding to each $St_{c,m}$ and how it changes with increasing St_c. It is observed that $|\lambda_m|$ generally decreases with higher $St_{c,m}$ values, a trend that remains consistent across different St_c ranges. However, the values of $|\lambda_m|$ corresponding to each mode number increase as St_c varies from 0.32 to 0.56. Notably, Modes 1, 2, and 3 exhibit a relatively higher percentage increase compared to Modes 4 and 5. Additionally, $|\lambda_4|$ and $|\lambda_5|$ reach saturation beyond $St_c = 0.48$ (see Figure 5(b)).

CONCLUSION

The transition from spanwise instability of primary LEV rollers to the formation of hairpin-like structures is observed

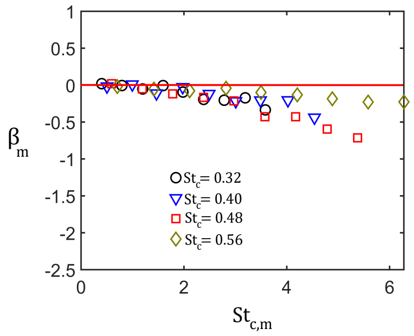

(a)

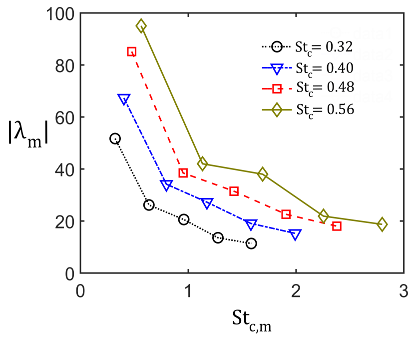

(b)

Figure 5: (a) Growth rates identified for first 9 modes excluding the Stationary mode (Mode 0). Horizontal axis represents the corresponding mode frequency ($St_{c,m}$) for each mode. The cases correspond to increasing St_c from 0.32 to 0.56. (b) Modulus calculated for first 5 energetic modes, excluding the stationary mode (Mode 0), at increasing St_c.

in the wake of an oscillating foil as St_c increases within the range of 0.32 to 0.56. This development of secondary streamwise vortical structures occurs alongside previously identified hairpin-like pairs originating from the core vorticity outflux of deforming secondary *LEV* (Verma *et al.*, 2023; Verma & Hemmati, 2023). At $St_c = 0.32$, there is no significant temporal amplification of vortex undulations and spanwise dislocations, preventing the transition to a second system of hairpin-like vortical structures. However, beyond $St_c = 0.32$, undulations intensify as the *LEV* advects in the wake, leading to vortex tearing at localized spanwise locations along the roller. Consequently, the *LEV* itself transforms into the second hairpin-like system that evolves alongside the pre-existing hairpin-like structures. The amplification of undulations at $St_c > 0.32$ is associated with enhanced vortex compression around the upstream regions neighboring primary $LEVs$, coinciding with the presence and growth of counter-rotating $TEVs$ that contribute to intensifying axial strain fields. The increasing circulation of $TEVs$ at higher St_c further accelerates the compression intensification, facilitating the early growth of the streamwise secondary hairpin-like system from the primary LEV. The stability analysis, and reduced order modeling using DMD, reveal the neutrally stable nature of the modes that remain consistent for the wakes with either a single or dual systems of secondary hairpin-like structures.

REFERENCES

Chiereghin, N., Bull, S., Cleaver, D. J. & Gursul, I. 2020 Three-dimensionality of leading-edge vortices on high aspect ratio plunging wings. *Physical Review Fluids* **5** (6), 064701.

Deng, Jian & Caulfield, C. P. 2015 Three-dimensional transition after wake deflection behind a flapping foil. *Physical Review E - Statistical, Nonlinear, and Soft Matter Physics* .

Hemati, Maziar S., Williams, Matthew O. & Rowley, Clarence W. 2014 Dynamic mode decomposition for large and streaming datasets. *Physics of Fluids* **26** (11), 111701.

Leweke, Thomas, Le Dizès, Stéphane & Williamson, Charles H.K. 2016 Dynamics and Instabilities of Vortex Pairs.

Leweke, T. & Williamson, C. H.K. 1998 Cooperative elliptic instability of a vortex pair. *Journal of Fluid Mechanics* .

Mittal, R. & Balachandar, S. 1995 Generation of streamwise vortical structures in bluff body wakes. *Physical Review Letters* .

Mohan, Arvind T., Gaitonde, Datta V. & Visbal, Miguel R. 2016 Model reduction and analysis of deep dynamic stall on a plunging airfoil. *Computers and Fluids* **129**, 1–19.

Ortega, J. M., Bristol, R. L. & Savas, Ö. 2003 Experimental study of the instability of unequal-strength counter-rotating vortex pairs. *Journal of Fluid Mechanics* **474** (474), 35–84.

Ryan, Kris, Butler, Christopher J. & Sheard, Gregory J. 2012 Stability characteristics of a counter-rotating unequal-strength Batchelor vortex pair. *Journal of Fluid Mechanics* **696**, 374–401.

Schaeffer, Nathanaël & Le Dizés, Stéphane 2010 Nonlinear dynamics of the elliptic instability. *Journal of Fluid Mechanics* **646**, 471–480.

Schnipper, Teis, Andersen, Anders & Bohr, Tomas 2009 Vortex wakes of a flapping foil. *Journal of Fluid Mechanics* .

Son, O., Gao, A. K., Gursul, I., Cantwell, C. D., Wang, Z. & Sherwin, S. J. 2022 Leading-edge vortex dynamics on plunging airfoils and wings. *Journal of Fluid Mechanics* **940**, A28.

Sun, Liping, Deng, Jian & Shao, Xueming 2018 Three-dimensional instabilities for the flow around a heaving foil. *Physical Review E* .

Verma, Suyash & Hemmati, Arman 2020 Performance of overset mesh in modeling the wake of sharp-edge bodies. *Computation* .

Verma, Suyash & Hemmati, Arman 2021 Evolution of wake structures behind oscillating hydrofoils with combined heaving and pitching motion. *Journal of Fluid Mechanics* **927**, A23.

Verma, Suyash & Hemmati, Arman 2023 Influence of kinematics on the growth of secondary wake structures behind oscillating foils. *International Journal of Heat and Fluid Flow* **102**, 109146.

Verma, Suyash, Khalid, Muhammad Saif Ullah & Hemmati, Arman 2023 On the association of kinematics, spanwise instability and growth of secondary vortex structures in the wake of oscillating foils. *Proceedings of the Royal Society A* **479** (2276).

Visbal, Miguel R. 2009 High-fidelity simulation of transitional flows past a plunging airfoil. *AIAA Journal* .

Williamson, C. H.K. 1996 Three-dimensional wake transition. *Journal of Fluid Mechanics* .

Wu, Jie-Zhi, Ma, Hui-Yang & Zhou, Ming-De 2006 *Vorticity and Vortex Dynamics*, p. 776.

Zheng, Hongyu, Xie, Fangfang, Zheng, Yao, Ji, Tingwei & Zhu, Zaoxu 2019 Propulsion performance of a two-dimensional flapping airfoil with wake map and dynamic mode decomposition analysis. *Physical Review E* **99** (6), 063109.